Materials Chemistry and Physics 225 (2019) 192–199

Contents lists available at ScienceDirect

Materials Chemistry and Physics

journal homepage: www.elsevier.com/locate/matchemphys

Enhanced energy density and stability of self-assembled cauliflower of Pd doped monoclinic WO_3 nanostructure supercapacitor

Shobhnath P. Gupta[a,1], Vandana B. Patil[b,1], Nilesh L. Tarwal[c], Shekhar D. Bhame[d], Suresh W. Gosavi[e], Imtiaz S. Mulla[f], Dattatray J. Late[g], Sharad S. Suryavanshi[b], Pravin S. Walke[a,*]

[a] National Centre for Nanosciences and Nanotechnology, University of Mumbai, Mumbai, 400098, Maharashtra, India
[b] School of Physical Sciences, Solapur University, Solapur, 413255, Maharashtra, India
[c] Lal Bahadur Shastri Mahavidyalaya, Satara, 415002, Maharashtra, India
[d] Symbiosis Institute of Technology, Symbiosis International University, Lavale, Pune, 412115, Maharashtra, India
[e] Department of Physics, Savitribai Phule Pune University, Pune, India
[f] Emeritus Scientist (CSIR), Centre for Materials for Electronic Technology (C-MET), Pune, 411008, Maharashtra, India
[g] Physical and Materials Chemistry Division, CSIR-National Chemical Laboratory, Dr. Homi Bhabha Road, Pashan, Pune, 411008, Maharashtra, India

HIGHLIGHTS

- Pristine WO_3 and Pd doped WO_3 is synthesized by simple hydrothermal method.
- The WO_3 cabbage morphology converted into WO_3 cauliflower by Pd doping.
- The greater surface area, crystallinity and conductivity are observed by doping.
- Almost four times higher specific capacitance is realized in WO_3 cauliflower.
- The excellent stability almost ten times higher is achieved in WO_3 cauliflower.

GRAPHICAL ABSTRACT

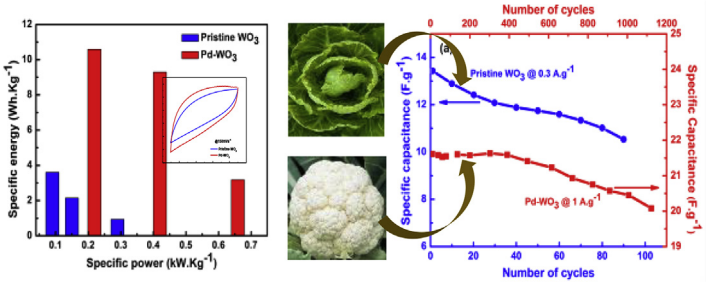

ARTICLE INFO

Keywords:
Pseudocapacitors
Tungsten oxide
Nanosheets
Nanobrick
Specific capacitance
Energy density

ABSTRACT

Enhanced electrochemical performance of WO_3 nanostructures by engineering their morphology, structural and surface defect at nanoscale is feasible. Herein we report the effect of Pd doping on the morphological and electrochemical properties of WO_3 at nanoscale prepared by a simple hydrothermal method. The synthesized pristine WO_3 (cabbage like morphology) and Pd doped WO_3 (cauliflower like morphology) are examined by using XRD, XPS, Raman spectra, BET, FE-SEM, TEM. The morphological investigation shows the effective rebuilding of nanosheets assembled cabbage shaped pristine WO_3 into nanobricks assembled cauliflower shaped Pd doped WO_3 with improvement in crystallinity, surface area and conductivity. As a result, the enhancement in the electrochemical performance of cauliflower shaped Pd-WO_3 is recorded four times higher specific capacitance than pristine WO_3. Additionally, the excellent cyclic stability (almost ten times higher than pristine WO_3) up to 1100 cycles with nearly 86.95% capacity retention is observed in Pd-WO_3 attributed to Pd content and highly modified structural arrangement.

* Corresponding author.
E-mail address: pravin.w@nano.mu.ac.in (P.S. Walke).
[1] These authors contributed equally.

https://doi.org/10.1016/j.matchemphys.2018.12.077
Received 21 August 2017; Received in revised form 18 November 2018; Accepted 10 December 2018
Available online 27 December 2018
0254-0584/

1. Introduction

Increasing energy demands certainly required eco-friendly, cheap and sustainable energy sources and suitable energy saving strategy using efficient energy generation, storage and low power consumption devices etc. [1]. Contributions of energy storage devices are increasing consistently in daily life through numerous resources such as home appliances, portable electronic devices, electric vehicles etc. [2]. Electrochemical energy storage devices namely batteries and super-capacitors are commercially available, which needs to further boost their performance along with cost reduction, increasing power and/or energy density, miniaturization and low weight, long life etc. in order to satisfy the market requirements. Supercapacitors (SCs) with enhanced energy density, power density and higher stability are highly desired in the portable electronics and electric vehicles [3–5]. Depending on the charge storage mechanism, the SCs are identified either pseudocapacitors (PCs) or electric double-layer capacitors (EDLCs). In PCs, charge accumulation occurs due to a faradic reaction at the electrode and electrolyte interface, whereas in EDLCs, charge accumulation occurs due to a non-faradic reaction at the surface of the carbon and related porous materials. Carbon-based EDLCs offer higher power density and good cyclic stability but their application in supercapacitor is limited due to low energy density. Generally transition metal oxides (WO_3, MnO_2, RuO_2, and NiO etc.) attracted attention of the researcher's due to pseudo-capacitive nature, which projects increasing energy density without compromising high power or cyclic life [6,7].

Many transition metal oxides have been studied comprehensively owing to their improved capacitance value occurs from rapid and reversible redox reaction. However, it has some limitations in commercial viewpoint; for example, RuO_2 is expensive and poisonous character, MnO_2 have lower electrical conductivity and ionic conductivity in spite of their low cost and adequate pseudo-capacitor performance. To overcome these limitations, electrode materials were loaded on conductive substrate such as graphene, metal foils, CNTs, porous metal, activated porous carbon, etc. [8–13] to improve the performance, however it is not appropriate for bulk production. Additionally at slow charging/discharging rates, supercapacitor exhibits the superior stability and better performances but it is really challenging to accomplish similar consequences at high rates. In this context, controlled doping and/or surface functionalization of metal oxides have been found to show higher capacitance value, wide working potential window, and increased stability, even without any conducting support [14–16].

The advantage of tungsten oxide (WO_3) is its multiple oxidation states, lower cost and the high intrinsic density ($> 7\ g\ cm^{-3}$), qualifying WO_3 as an alternative electrode material for miniaturized SCs system, though the cost and stability is comparable to MnO_2. Hence the criterion required for high performance WO_3 electrodes are (1) improved electrical conductivity of WO_3 by reducing total internal resistance and (2) increasing surface area of WO_3 nanostructure [17–19]. The suitable metal doping will enhance the electrical conductivity as a result of tuning fermi energy level, which increases electron density as well as surface area, by tuning the morphology [17–19]. The doping concentration plays crucial role in the modification of structures, morphology and surface area eventually.

Herein, we report the consequence of 3% wt. Pd doping on morphology, structural and electrochemical performance of WO_3 nanostructures for supercapacitor application. The results exhibit that Pd doping transform nanosheet assembled cabbage shaped pristine WO_3 into nanobricks assembled Pd-WO_3 cauliflower via induced defects, replacement of metallic tungsten by Pd as well as formation of bonds between Pd and oxygen into WO_3 matrix. Besides the morphological change; the better surface access area and improved electrical conduction are the merits of Pd-WO_3 responsible for enhanced electrochemical performance. Hence it is highly significant for futuristic design of crystal structure and surface defect engineering of Pd-WO_3 in order to enhance supercapacitor performance.

2. Experimental

All chemicals used were analytical reagent grade and the solutions were prepared using double distilled water. The sodium tungstate dihydrate ($Na_2WO_4{\cdot}2H_2O$) was purchased from Tianjin City Regent Chemicals Co., $PdCl_2$ from Merck. The oxalic acid ($H_2C_2O_4$) and hydrochloric acid (HCl) was procured from Sigma Aldrich, India.

Synthesis of pristine WO_3: The tungsten precursor solution was prepared by dissolving 3.28 g $Na_2WO_4{\cdot}2H_2O$ in 75 ml distilled water. The final pH value of the solution was regulated in two steps. Firstly, the solution was acidified through adding 3 M HCl with subsequent magnetic stirring. Second step, 2.64 g $H_2C_2O_4$ was added until a translucent homogeneous solution obtained, which adjusts the pH value up to 2.

Synthesis of Pd doped WO_3: Few drops of 3 M HCl were added to 25 ml solution of distilled water containing (1.73 g) $PdCl_2$ to facilitate dissolution along with simultaneous stirring for 6–7 h, till the solution becomes light brown in color. This brownish solution further mixed with subsequent stirring for 2 h into the initial precursor solution (prepared for pristine sample synthesis); until yellow transparent mixture solution obtained.

The both precursor solutions were subsequently stirred for 30 min, and then transferred into Teflon-lined autoclave. Further hydrothermal growth was prepared at 170 °C for 24 h in furnace. Finally the autoclave was naturally cooled to room temperature followed by repeated deionized (DI) water washing and calcination at 400 °C for 2 h.

3. Results and discussion

3.1. Characterization of pristine WO_3 and Pd-WO_3

The overall morphology of pristine WO_3 and Pd-WO_3 are shown in the Fig. 1(a–d). Fig. 1 (a) representing several nanosheets self-assembled into cabbage like configuration, for better insight cabbage picture is displayed in the inset of Fig. 1 (a). The enlarged view in Fig. 1 (c) clearly shows nanosheets having thickness in the range of 15–30 nm; which represents disrupted outer leaves of cabbage. Fig. 1 (b) and (d) demonstrates nanobricks assembled into cauliflower shape of Pd-WO_3 that can be linked with the cauliflower picture shown in the inset of Fig. 1 (b). The large number of bricks are present with dimensions i.e. length in the range of 500–700 nm, and 50–120 nm almost equal width and breadth.

The SEM images clearly express morphological changes with respect to Pd doping. The electro-negativity of W, 2.36 is higher than that of Pd, 2.20, Hence W is chemically more active than Pd which limits two dimensional growths [20] by reducing growth rate and directed three dimensional nanobricks structure. In addition, it is expected that the larger ionic radius of Pd (0.78 Å) compared to ionic radius of W^{6+} (0.56 Å). Probably, most of the Pd may be distributed around grain boundaries of WO_3 allowing 3D growth rather than uni and/or bi-directional growth at Pd-WO_3 [20,21]. The growth of 3% Pd doped WO_3 leads to a significant modification of growth kinetics promoting 3D growth at the nucleation sites [22].

The effect of Pd doping on surface area of the Pd-WO_3 nanostructures were studied using nitrogen adsorption isotherms and examined by Brunauer-Emmette-Teller (BET) measurements (see in S1, S2). BET results depict a surface area of 26.5 m^2/g for pristine cabbage shaped WO_3 due to the sheet-like structures and a higher surface area 32.2 m^2/g after doping with Pd, that can be assigned to the agglomerated nanobricks with slit like larger pore diameter of Pd-WO_3 in the agreement with the FE-SEM.

The detailed morphological and structural features of the WO_3 and Pd-WO_3 are obtained by TEM and HRTEM as shown in Fig. 2 (a) and (b) respectively. The obtained nano-sheet and nanobricks are in good agreement with FESEM results as shown in Fig. 1(a) and (b) respectively. The selected area electron diffraction (SAED) patterns of pristine

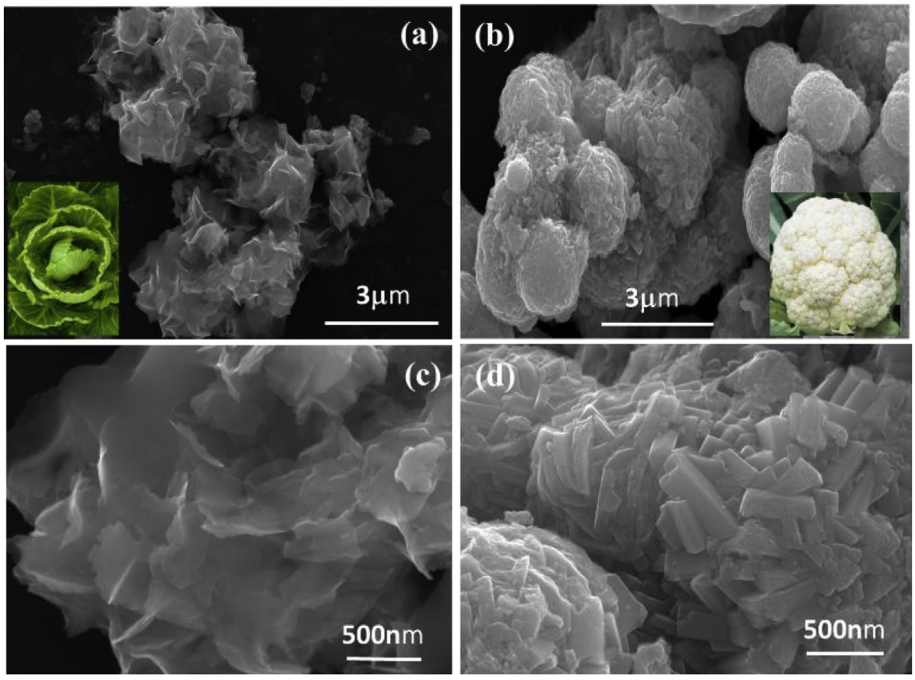

Fig. 1. FESEM images of (a) the Pristine WO_3, cabbage photograph shown in the inset, (b) Pd-WO_3, cauliflower photograph shown in the inset and (c-d) highly magnified FESEM images of pristine WO_3 and Pd-WO_3 respectively.

WO_3 indicate polycrystalline nature shown in the inset of Fig. 2 (a). The SAED pattern in the inset of Fig. 2 (a) showed bright spots on diffraction rings agrees with the 002, 020, 220 reflections of the monoclinic WO_3 and large diffraction rings correspond to the weak reflections. The high degree of crystallinity of Pd-WO_3 is confirmed by the SAED shown in the inset of Fig. 2(b). The additional small low intense white spots in the SAED pattern are originated from defects states or grain boundaries/mixed phase of Pd and WO_3. The inter-planar distance was computed to be 0.39 nm, which corresponds to the (200) reflection in the monoclinic phase of Pd-WO_3 nanobricks shown in Fig. 2 (c).

Fig. 3 (a) shows X-ray diffraction patterns of WO_3 cabbage and Pd-WO_3 cauliflower represented with the strong and sharp diffraction peaks indicate good crystalline nature. It also confirms monoclinic phase of WO_3 matching (JCPDS Card No. 89-4476) the diffraction peaks at $2\theta = 23.1^{\circ}$, 23.5° and 24.3° with the (002), (020) and (200) reflection respectively. The Pd-WO_3 sample shows marginally intensive peak so as increase crystalline nature supports TEM investigation. The PdO peak at 41.5° is overlapped with WO_3 peak in (222) crystallographic direction. The evidence of PdO is clearly shown by XPS analysis, which will be discussed later. No significant structural changes or secondary phases such as tungsten dioxide or metallic tungsten could be observed in XRD with Pd doping as seen in TEM and SAED. The calculated crystalline size by Debye-Scherrer's equation for both the samples is between 39 and 65 nm expecting crystalline size decreases with Pd concentration [20–22].

The results verified the crystal structure with monoclinic nature for both WO_3 cabbage and Pd-WO_3 cauliflower from the TEM, SAED and XRD. The increased crystallinity enhances the conductivity and bond strength in Pd-WO_3 is an added advantage for the supercapacitor application. Fig. 3 (b) shows the Raman spectrum of the pristine WO_3 cabbage and Pd-WO_3 cauliflower. Raman spectra of pristine WO_3 cabbage shows weak peaks of bending and stretching mode with a single high intense peak of stretching vibrational bands at 802 cm^{-1}. Pd doping clearly enhances surface Plasmon contribution signifies the modification of fermi energy levels and electronic configuration. Hence the Raman spectrum of Pd-WO_3 shows the sharp bands at 811 cm^{-1}, 675 cm^{-1}, 325 cm^{-1}, 241 cm^{-1} matching with monoclinic tungsten oxide that supports XRD results. The band at 240 cm^{-1} corresponds to bending mode of O-W-O, and the stretching modes of W-O-W at the bands 675 cm^{-1} and 811 cm^{-1} are observed, which is very weak in pristine WO_3 planar sheet signifies less strength [23]. The low frequency peak at 147 cm^{-1} ascribed to the O-O deformation and 325 cm^{-1} credited to W-O deformation modes [24], representative alignment of the anisotropic atoms on the surface. Additionally shifting of W = O band peak of pristine WO_3 from 960 cm^{-1}–939 cm^{-1} indicates vibrational Pd = O band related with the doping of Pd atoms

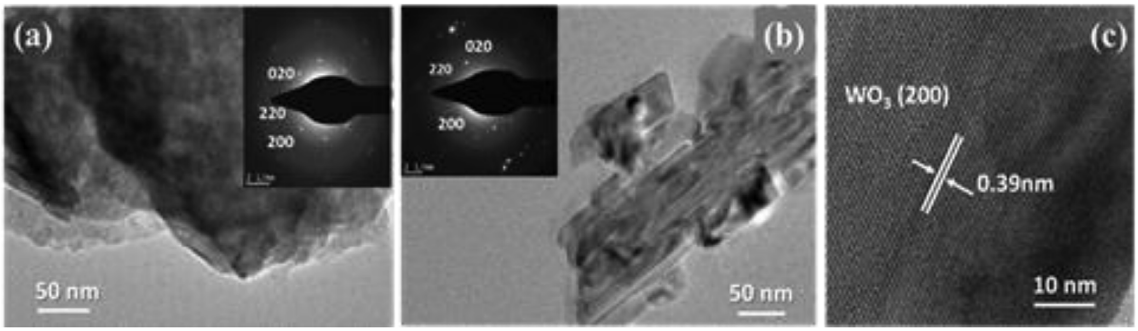

Fig. 2. TEM images (a) Pristine WO_3, (b) Pd-WO_3, inset of (a) SAED pattern of pristine WO_3 and the inset of (b) SAED of Pd-WO_3, (c) HRTEM image of Pd-WO_3.

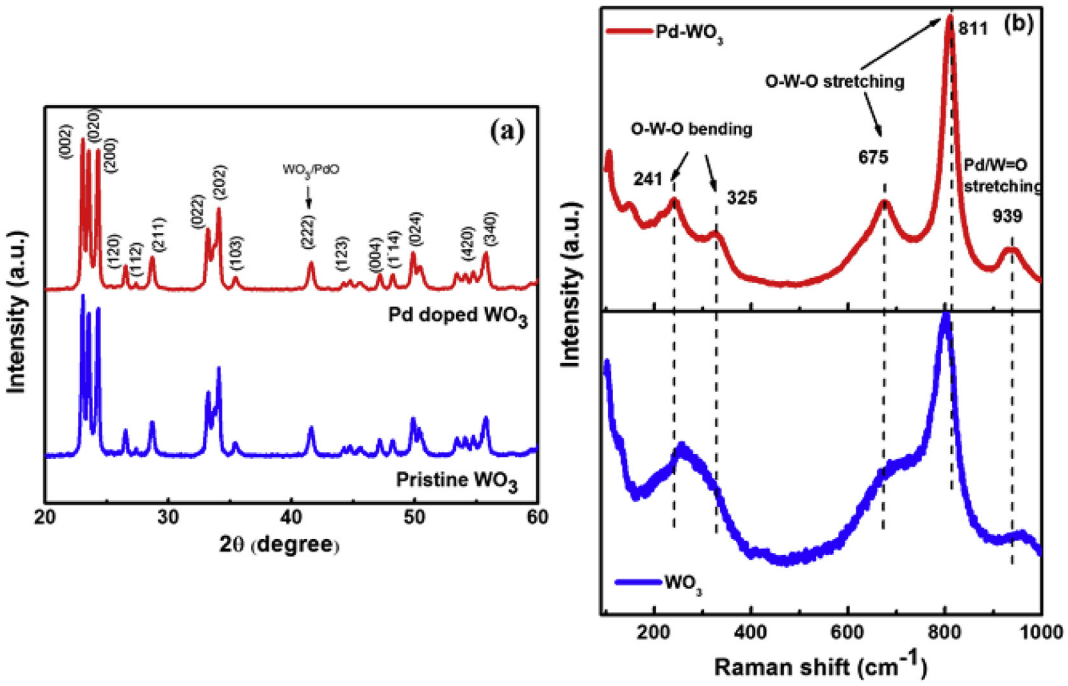

Fig. 3. (a) XRD patterns of pristine WO_3 and Pd-WO_3. (hkl) parameters refer to the monoclinic phase of WO_3 (b) Raman spectra of pristine WO_3 and Pd-WO_3.

into WO_3 [25,26]. Thus Pd doping promotes the stretching, bending and deformation leads to rearrangement of the structure.

The composition analysis and valence states of WO_3 cabbage and Pd-WO_3 cauliflower are examined by XPS. A typical survey spectrum of the pristine WO_3 and 3% Pd-WO_3 (see in S3) shows the co-existence of W and Pd in the Pd-WO_3. The detailed XPS spectra of W-4f, O-1s in both the samples and Pd-3d with corresponding peak fitting are presented in Fig. 4. The pristine WO_3 cabbage indicates the well-resolved peaks fitted at the binding energy of 35.38, 37.7 and 40.94 eV signifying the spin–orbit split peaks of W $4f_{7/2}$, W $4f_{5/2}$ and W $4f_{3/2}$, respectively as seen in Fig. 4 (a) [27,28]. The peaks at the higher binding energy (35.38 eV and 37.7 eV) in the W $4f_{7/2}$ and W $4f_{5/2}$ doublet representing W^{6+}, and those at lower binding energy 33.9 eV and 36.07 eV representing W^{5+} [28–30]. Fig. 4(b) displays peaks shift (W^{6+} and W^{5+}) to the higher binding energies (36.3 eV and 38.53 eV) with Pd doping due to charge imbalance of W-O [31]. Additionally, interactions between W and Pd atoms cause an up shift in the binding energy via band gap tuning which locally modify the barrier height to regulate emission of photoelectron from the sample surface [27].

Fig. 4(c) shows O1s spectra of WO_3 cabbage have two peaks that fitted to lattice oxygen at 530.3eV and the hydroxyl groups at 531.0 eV. Nevertheless Fig. 4(d) shows up-shift of the lattice oxygen to 530.1 eV and a new peak at 528.7eV arising from W-O-Pd in Pd-WO_3 cauliflower. Lower energy peaks in W4f associated with W^{5+} indicates oxygen

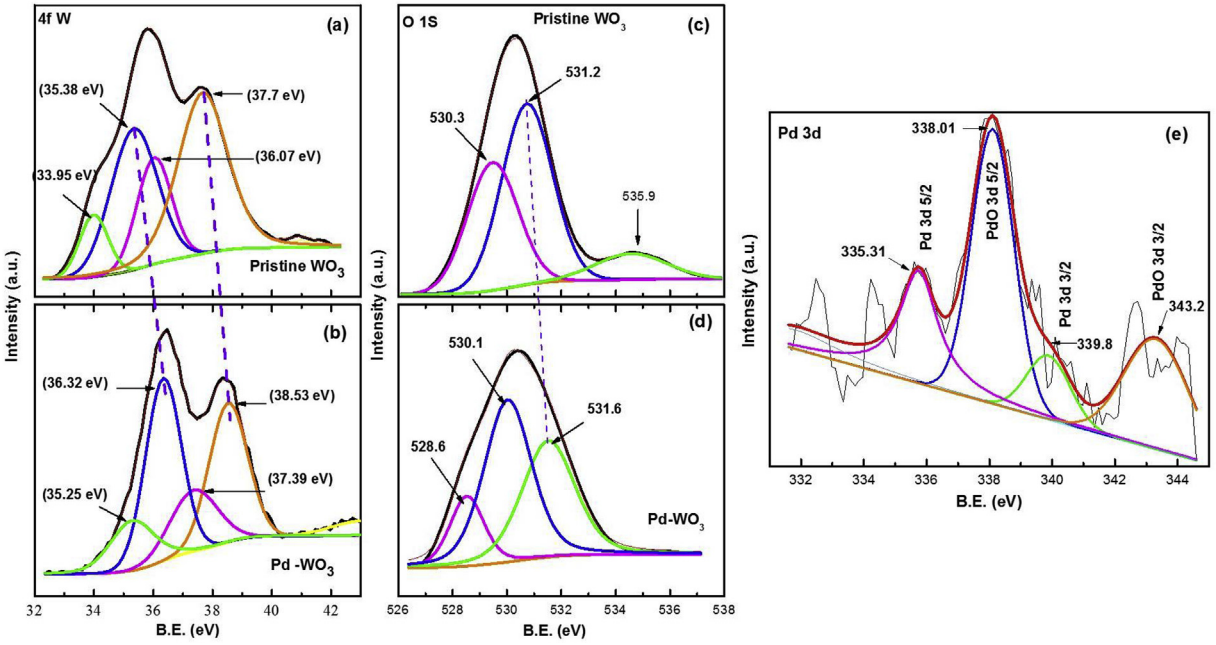

Fig. 4. XPS Spectra (*a*) W 4f of pristine WO_3, (*b*) W 4f of Pd-WO_3, (*c*) O 1s of pristine WO_3, (*d*) O 1s of Pd-WO_3, (*e*) Pd 3d of Pd-WO_3.

vacancies in both the samples which was confirmed by the O peak at higher binding energy 535 eV, even higher in case of Pd-WO_3 related to oxygen atoms. Additionally, O 1s spectra in pristine WO_3 show the contribution of lattice oxygen is less than the hydroxyl group, and conversely the lattice oxygen contribution is greater than the hydroxyl group in the Pd-WO_3. Hence the more oxygen bonding with the lattice occurs in Pd-WO_3 due to PdO formation. The shifts of both W4f and O1s in Pd-WO_3 nanobricks specify that the modification of W and O atoms originated from the W-O and O-O bond deformation by Pd doping, coincident with the Raman investigation.

The XPS spectrum of Pd 3d of 3% Pd-WO_3 is shown in Fig. 4(e). The peaks at a binding energy of 335, 339.8 eV representing metallic Pd $3d_{5/2}$ and Pd $3d_{3/2}$ respectively and peak at 338.01, 343.2eV representing PdO $3d_{5/2}$ and PdO $3d_{3/2}$, respectively, marks the existence of Pd and formation of PdO. Although the oxidized palladium has major contribution than metallic Pd as the metallic Pd has a very weak signal, which is consistent with the Raman spectra [20,31]. Thus possibility of sorption of hydrogen at Pd is negligible and stability would be more as compare to bare Pd. Moreover, the difference in O1s spectrum had shown in Fig. 4 (c) and (d).

3.2. Electrochemical performance

Electrochemical measurements were recorded in a typical three-electrode system in 1 M Na_2SO_4 solution with WO_3 nanostructure coated glassy carbon electrode, a Pt electrode and an Ag/AgCl electrode as the working electrode, counter electrode and reference electrode, respectively. Cyclic voltammetry (CV) were carried out in potential window of −0.7 to 0.1 V using 1 M Na_2SO_4. Generally, WO_3 electrode stores charges by two specific ways, electric double layer at the electrode/electrolyte interface and second through redox reactions at electrode surface.

Fig. 5 (a) and (b) exhibits the CV curves of WO_3 cabbage and Pd-WO_3 cauliflower respectively at various scan rates in a broad voltage window from −0.7 to 0.1 V. Pseudocapacitive performance of both the materials are clearly evident from the non-ideal rectangular shapes of CV curves; the observed redox peaks exhibit the faradic nature of the WO_3 [32]. From the CV curves, it can be distinguished that the Pd-WO_3 cauliflower display highest area under the curve compare to WO_3 cabbage. Thus Pd-WO_3 is suitable for the better electrochemical performance. The specific capacitance (Cs, $F.g^{-1}$) values were also calculated from the results of CV curve. Fig. 5 (c) shows the calculated specific capacitance vs scan rate for both the materials. The linear dependence of specific capacitance with the scan rate is observed, the specific capacitance decreases with increasing scan rate. In case of Pd-WO_3 cauliflower, the rate of reducing specific capacitance at higher scan rate is very less or almost stable as compare to pristine WO_3 cabbage. The ion exchange mechanism supports the decreasing specific capacitance with increasing scan rate [33]. At low scan rate, ionic diffusion is higher due to slow intercalation whereas ionic diffusion is less at fast scan rate. Hence lower degree of ionic intercalation in to the electrode material and fast reaction reduces the specific capacitance value. The cauliflower morphology has higher surface area with large pore diameter creates cavity for electrolyte that offers higher electroactive area as well as reduce diffusion length even at high scan rate as compare to pristine WO_3 cabbage. Moreover the improved conductivity due to Pd doping enhances electrochemical performance [34].

The galvonostatic charge/discharge (GCD) curves of WO_3 (Fig. 5 (d)) and Pd-WO_3 (Fig. 5 (e)) were recorded at different current densities. Fig. 5 (d) clearly shows the IR drop during discharge cycle signifying intrinsic resistance of cabbage WO_3. Moreover the Pd-WO_3 cauliflower has increased the discharge time with negligible IR drop and relatively higher specific capacitance owing to the improved electrical conductivity of the Pd-WO_3 by Pd doping and improved crystallinity, thereby facilitating the easy transfer of electrons during the charge/discharge process. Furthermore Fig. 5(f) shows specific capacitance values of Pd-WO_3 cauliflower is almost three times higher than pristine WO_3 cabbage at different current densities.

Fig. 6 (a) depicts the comparative CV curves of pristine WO_3 and Pd-WO_3 at a scan rate of 150 mV s^{-1}. It is remarkable that although there is no significant change in operational voltage window, the current density of the Pd-WO_3 cauliflower has increased considerably. Similarly, Fig. 6 (b) indicates the comparison of the GCD curves at 0.5 A g^{-1} for both WO_3 and Pd-WO_3. The Pd-WO_3 based electrode showed

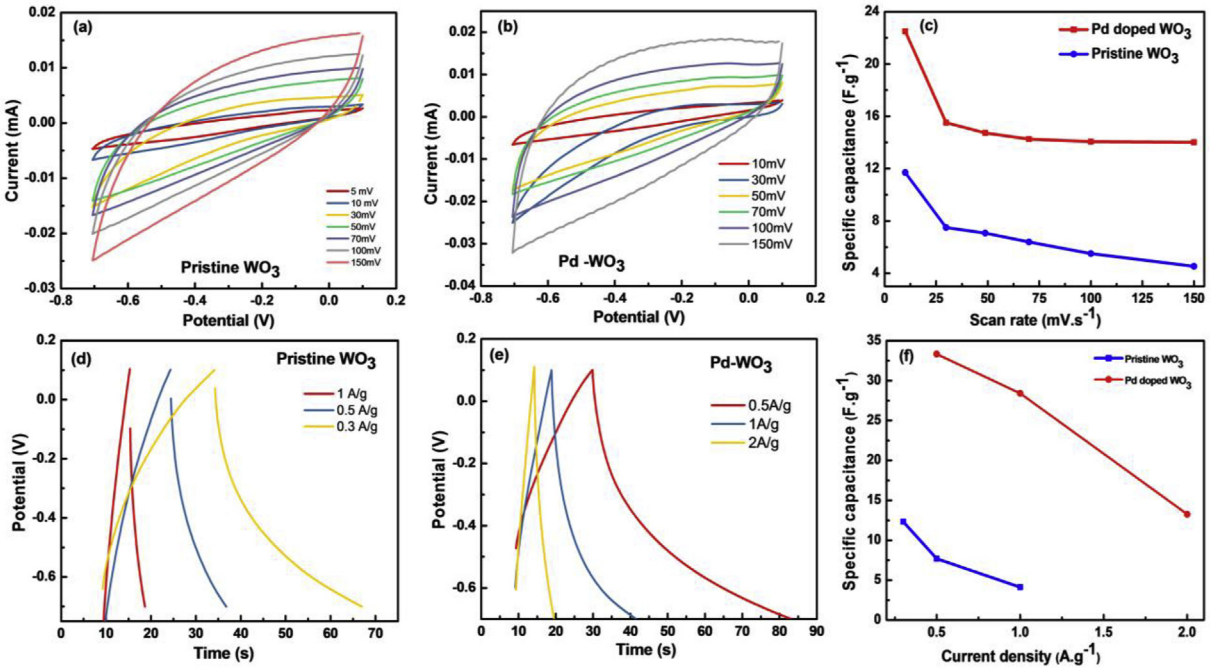

Fig. 5. CV curves at scan rates varying from 5 mV s^{-1} to 150 mV s^{-1} (a) and (b) for pristine WO_3 cabbage and Pd-WO_3 cauliflower respectively, (c) and (f) specific capacitance calculated from CV curves with respect to scan rate and GCD curve at different current densities respectively (d) and (e) GCD curves at different current densities of the pristine WO_3 cabbage and Pd-WO_3 cauliflower respectively.

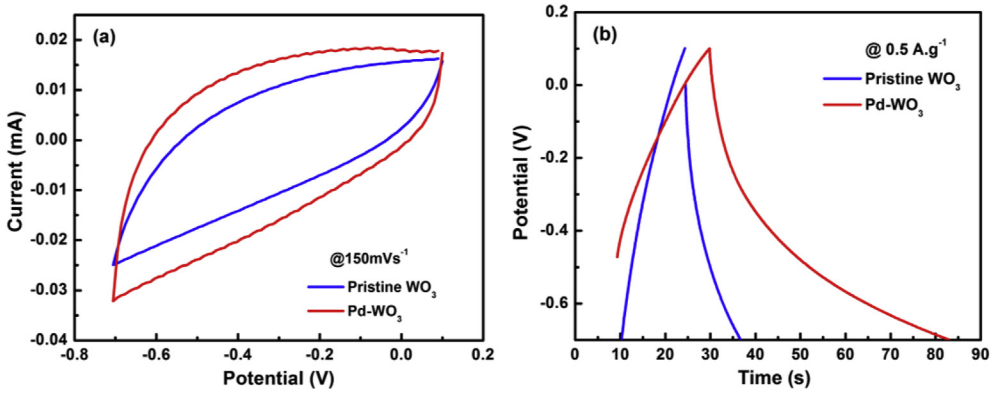

Fig. 6. (a) The comparative CV performance of the pristine WO_3 cabbage and Pd-WO_3 cauliflower at 150 mV s^{-1} and (b) The comparative GCD performance of the pristine WO_3 cabbage and Pd-WO_3 cauliflower at 0.5 A g^{-1}.

substantially longer (almost double) discharge time as compared to the pristine WO_3, which clearly reveals larger specific capacitance. The specific capacitance values from GCD for the WO_3 cabbage is 12.32 F g^{-1} at 0.3 A g^{-1} and for Pd-WO_3 cauliflower is 33.34 F g^{-1} at 0.5 A g^{-1} which is almost three and half times higher value than WO_3 cabbage.

This pseudocapacitance is owing to fast and reversible faradaic reactions that have been demonstrated in many studies, and which involve the electrochemical inter-conversion between W^{6+} and W^{5+} in the solid, and corresponding insertion of cations, Na^+, from the electrolyte [36]. As expected from the XPS, increasing oxygen vacancies might create due to PbO formation; therefore W^{5+} contribution is higher in Pd-WO_3 that enhances the pseudo-capacitance [37]. At current density 0.5 A g^{-1}, it clearly shows drastic difference in capacity of the materials i.e. 7.5 C g^{-1} for pristine WO_3 cabbage and 27 C g^{-1} for Pd-WO_3 cauliflower. Thus Pd doping into WO_3 reveals more than three times higher capacity.

The enhanced electrochemical performance for Pd doped WO_3 electrode indicates that Pd extensively influences the capacitive behavior of WO_3 in the modified nanostructure. There are three more reasons for this enhancement: 1) The controlled assembly of Pd-WO_3 structures which enables simple transfer of electrolyte ions by reducing the internal resistance and enhance reversible redox reaction, 2) The Pd-WO_3 provides channel to electron by mean of crystalline orientation indicated by Raman, XRD and TEM and 3) increasing surface area by mean of large slit type pore diameter presented by BET, which can serve as cavity for electrolyte that reduce diffusion length and promotes intercalation of ions. Therefore near surface intercalation was contributing to pseudocapacitance in the crystalline, which is not the case of amorphous materials [35–37].

A Ragone plot is shown in Fig. 5 (f). The gravimetric energy density and power density of the Pd-WO_3 cauliflower and WO_3 cabbage was determined from GCD curves. The WO_3 cabbage exhibits low gravimetric energy density 3.5 Wh.kg^{-1} at power density of 110 W kg^{-1} whereas two plus half times enrichment in the specific energy 3.64 Wh.kg^{-1} at specific power 198 W.kg^{-1} of Pd-WO_3 cauliflower is recorded. The better electrical conductivity, increased surface area and advanced cauliflower assemblies due to Pd incorporation into WO_3 authenticates the enhanced performance.

Fig. 7(a) illustrates the cycling stability of the WO_3 cabbage and Pd doped WO_3 cauliflower investigated by GCD technique. WO_3 cabbage is persistent up to 100 GCD cycles at 0.3 A g^{-1}. Nevertheless Pd-WO_3 cauliflower structure shows 86.95% capacitance retention up to 1100 cycles at higher current density 1 A g^{-1}, which is much better than cabbage WO_3. It is important to note that even at higher energy density the cyclic stability was improved by almost ten times as compare to cabbage WO_3.

Fig. 7(b) shows the impedance plots of pristine WO_3 cabbage and Pd-WO_3 cauliflower. The inset of Fig. 7(b) shows the equivalent circuit for the Nyquist plots. In the circuit, R_S and R_{CT} are solution resistance and charge-transfer resistance, respectively. C is the capacitance and Z_W is the Warburg impedance. The intercept of impedance curve at the Z′-axis represents the equivalent series resistance (R_S) that includes electronic resistance of electrode, ionic resistance of electrolyte, and contact resistance. The WO_3 cabbage has a larger R_S value than Pd-WO_3 cauliflower due to intrinsic resistance contribution. Additionally an increasing electrical conductivity of the Pd-WO_3 is due to band gap alteration and decreases in R_S value.

The diameter of the semicircle on the impedance curve indicates the charge-transfer resistance (R_{CT}), which represents the resistance of the electro-chemical reaction on the interface of the electrolyte and electrode. The large semicircle of the pristine WO_3 cabbage electrode in the high-frequency region indicates a high ion resistance that is most likely caused by the sheets morphology and large diffusion path, higher internal resistance etc. In case of Pd-WO_3 cauliflower, the semicircle become clearer and its diameter shrinkage indicates increasing charge transport due to availability of multiple oxidation states of W. In the middle-frequency region, the more than 45° sloped curve known as the Warburg portion (Z_W) is closely related to the transport of electrolyte ions in the electrodes. The short Warburg region observed for the Pd-WO_3 cauliflower electrode during redox process reveals that electrolyte intercalated through cavity, which is formed by slit type pores of bricks assembled cauliflower; greatly facilitated the diffusion of the electrolyte ions through its short and straight meso-channels. The cauliflower Pd-WO_3 structures have a high BET area (32.2 m^2 g^{-1}), and the large pore sizes 138.2 nm (see in S2). It is well known that the high BET area could increase electroactive surface area and offers more active sites could enhance the intercalation, results reducing R_{CT} value.

Hence overall improved conductivity by Pd doping and increasing surface area and smooth charge transfers due to modification of chemical composition by Pd doping enhances electrochemical supercapacitive performance. The present investigation is highly useful for enhancement of the supercapacitors performance of WO_3 based composite materials [18,19] through replacement of Pd doped WO_3 nanostructures instead pure WO_3 nanostructures.

4. Conclusion

In summary, a simplistic and inexpensive hydrothermal method is used for the synthesis of WO_3 cabbage and Pd-WO_3 cauliflower configuration. Pd doping is effectively transformed nanosheets assembled cabbage of pristine WO_3 into nanobricks assembled cauliflower with effectively increasing crystallinity, surface area and conductivity of Pd-WO_3 nanobricks. The Pd-WO_3 cauliflower is representing excellent supercapacitive property with higher gravimetric energy density of 10.6 Wh.kg^{-1} at power density of 198 W kg^{-1}. Moreover, the doping of

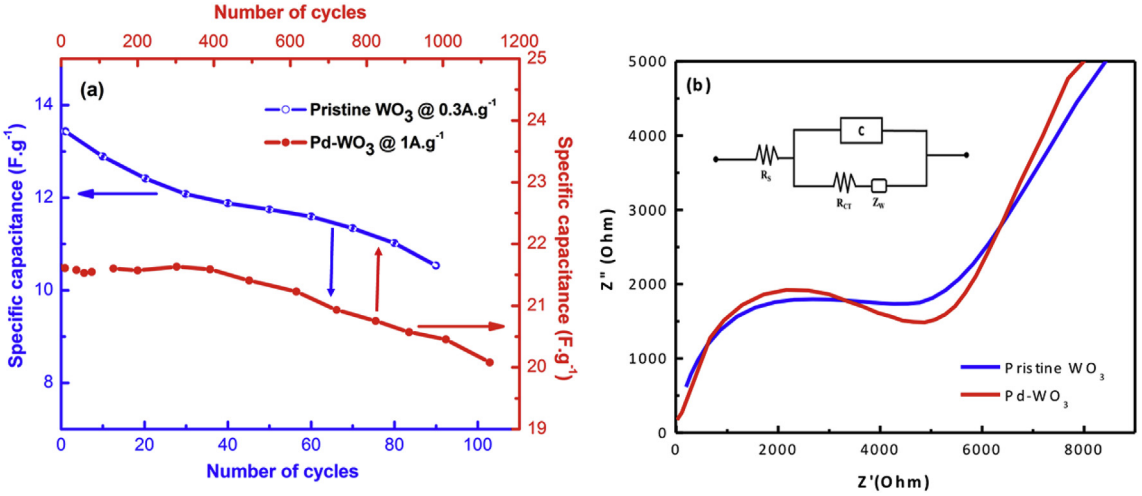

Fig. 7. (a) Cycle stability tested at 0.3 A g^{-1} for Pristine WO_3 cabbage and at 1 A g^{-1} for Pd-WO_3 cauliflower and (b) Nyquist plot of the pristine WO_3 cabbage and Pd-WO_3 cauliflower.

Pd promises an excellent strategy for structural and surface defect engineering to enhance capacitance almost four times up to 41 F g^{-1} accompanied by improved cycling stability, 86.95% retention even after 1100 cycles almost ten times more than pristine WO_3 cabbage. Hence Pd-WO_3 cauliflower is highly suitable for practical supercapacitor applications.

Acknowledgement

P. S. Walke is thankful to SERB- YSS/2015/001937 (Fast track young scientist research scheme) for financial support. D. J. Late acknowledges DST-Ramanujan Fellowship (Grant No. SR/S2/RJN-130/2012). S. P. Gupta thanks Mr. Shakeel Rahmaan for his assistance in electrochemical measurements. I. S. Mulla acknowledges CSIR, Delhi for granting him Emeritus Scientist Scheme.

Appendix A. Supplementary data

Supplementary data to this article can be found online at https://doi.org/10.1016/j.matchemphys.2018.12.077.

References

[1] Steven Chu, Arun Majumdar, Opportunities and challenges for a sustainable energy future, Nature 488 (2012) 294–303.
[2] Steve Sorrell, Reducing energy demand: a reviews of issues, challenges and approaches, Renew. Sustain. Energy Rev. 47 (2015) 74–82.
[3] B.E. Conway, Electrochemical Supercapacitors: Scientific Fundamentals and Technological Applications, Kluwer Academic/Plenum, New York, 1999.
[4] J.R. Miller, P. Simon, Materials science: electrochemical capacitors for energy management, Science 321 (2008) 651–652.
[5] P. Simon, Y. Gogotsi, Materials for electrochemical capacitors, Nat. Mater. 7 (2008) 845–854.
[6] S.H. Oh, L.F. Nazar, Direct synthesis of electroactive mesoporous hydrous crystalline RuO_2 templated by a cationic surfactant, J. Mater. Chem. 20 (2010) 3834–3839.
[7] T. Xue, C.-L. Xu, D.-D. Zhao, X.-H. Li, H.-L. Li, Electrodeposition of mesoporous manganese dioxide supercapacitor electrodes through self-assembled triblock copolymer templates, J. Power Sources 164 (2007) 953–958.
[8] F.S. Gergely, P. Kriszta, J. Csaba, R. Krishnan, On the electrochemical synthesis and charge storage properties of WO_3/polyaniline hybrid nanostructures, J. Solid State Electrochem. 19 (2015) 2741–2751.
[9] Y.-T. Kim, K. Tadai, T. Mitani, Highly dispersed ruthenium oxide nanoparticles on carboxylated carbon nanotubes for supercapacitor electrode materials, J. Mater. Chem. 15 (2005) 4914–4921.
[10] J.H. Jang, S. Han, T. Hyeon, S.M. Oh, Electrochemical capacitor performance of hydrous ruthenium oxide/mesoporous carbon composite electrodes, J. Power Sources 123 (2003) 79–85.
[11] G. Yu, L. Hu, M. Vosgueritchian, H. Wang, X. Xie, J.R. McDonough, X. Cui, Y. Cui, Z. Bao, Solution-processed graphene/MnO_2 nanostructured textiles for high-performance electrochemical capacitors, Nano Lett. 11 (2011) 2905–2911.
[12] X. Lang, A. Hirata, T. Fujita, M. Chen, Nanoporous metal/oxide hybrid electrodes for electrochemical supercapacitors, Nat. Nanotechnol. 6 (2011) 232-226.
[13] D. Liu, Q. Wang, L. Qiao, F. Li, D. Wang, Z. Yang, D. He, Preparation of nano-networks of MnO_2 shell/Ni current collector core for high-performance supercapacitor electrodes, J. Mater. Chem. 22 (2012) 483–487.
[14] S.R. Suryawanshi, V. Kaware, D. Chakravarty, P.S. Walke, M.A. More, K. Joshi, C.S. Rout, D.J. Late, Pt-nanoparticle functionalized carbon nano-onions for ultra-high energy supercapacitors and enhanced field emission behaviour, RSC Adv. 5 (2015) 80990–80997.
[15] J. Li, G. Zan, Q. Wu, Ultra-high-performance anode material for supercapacitors: self-assembled long Co_3O_4 hollow tube network with multiple heteroatom (C-, N- and S-) doping, J. Mater. Chem. 4 (2016) 9097–9105.
[16] H.Z. Chi, Y. Li, Y. Xin, H. Qin, Boron-doped manganese dioxide for supercapacitors, Chem. Comm. 50 (2014) 13349–13352.
[17] D. Wang, J. Li, X. Cao, G. Pang, S. Feng, Hexagonal mesocrystals formed by ultra-thin tungsten oxide nanowires and their electrochemical behaviour, Chem. Comm. 46 (2010) 7718–7720.
[18] X. Lu, T. Zhai, X. Zhang, Y. Shen, L. Yuan, B. Hu, L. Gong, J. Chen, Y. Gao, J. Zho, Y. Tong, Z.L. Wang, WO_{3-x}@Au@MnO_2 core–shell nanowires on carbon fabric for high-performance flexible supercapacitors, Adv. Mater. 24 (2012) 938–944.
[19] K. Nayak, A.K. Das, D. Pradhan, High performance solid-state asymmetric supercapacitor using green synthesized graphene-WO3 nanowires nanocomposite, ACS Sustain. Chem. Eng. 5 (2017) 10128–10138.
[20] L.F. Zhu, J.C. She, J.Y. Luo, S.Z. Deng, J. Chen, N.S. Xu, Study of physical and chemical processes of H2 sensing of Pt-coated WO3 nanowire films, J. Phys. Chem. C 114 (2010) 15504-11509.
[21] Z. Gu, H. Li, T. Zhai, W. Yang, Y. Xia, Y. Ma, J. Yao, Large-scale synthesis of single-crystal hexagonal tungsten trioxide nanowires and electrochemical lithium intercalation into the nanocrystals, J. Solid State Chem. 180 (2007) 98–105.
[22] S. Fardindoost, A. Irajizad, F. Rahimi, R. Ghasempour, Pd doped WO_3 films prepared by sol–gel process for hydrogen sensing Inter, J. Hydrogen Energy 35 (2010) 854–860.
[23] F.D. Hardcastle, I.E. Wachs, Determination of the molecular structures of tungstates by Raman spectroscopy, J. Raman Spectrosc. 26 (1995) 397–405.
[24] J.Y. Luo, S.Z. Deng, Y.T. Tao, F.L. Zhao, L.F. Zhu, L. Gong, J. Chen, N.S. Xu, Evidence of localized water molecules and their role in the gasochromic effect of WO_3 nanowire films, J. Phys. Chem. C 113 (2009) 15877–15881.
[25] M.P. Thi, G. Velasco, Raman study of WO_3 thin films, Solid State Ionics 14 (1984) 217–220.
[26] M.P. Thi, Microprobe study of enhanced Raman scattering effect on WO3/Ag thin films, Chem. Phys. Lett. 115 (1985) 130–133.
[27] F. Bussolotti, L. Lozzi, M. Passacantando, S.L. Rosa, S. Santucci, L. Ottaviano, Surface electronic properties of polycrystalline WO_3 thin films: a study by core level and valence band photoemission, Surf. Sci. 538 (2003) 113–123.
[28] M. Deepa, A.K. Srivastava, S.N. Sharma, Govind, S.M. Shivaprasad, Microstructural and electrochromic properties of tungsten oxide thin films produced by surfactant mediated electrodeposition, Appl. Surf. Sci. 254 (2008) 2342–2352.
[29] P. Yang, P. Sun, Z. Chai, L. Huang, X. Cai, S. Tan, J. Song, W. Mai, Large-Scale fabrication of pseudocapacitive glass windows that combine electrochromism and energy storage, Angew. Chem. Int. Ed. 53 (2014) 11935–11939.
[30] S. Cong, Y.Y. Tian, Q.W. Li, Z.G. Zhao, F.X. Geng, Single-crystalline tungsten oxide quantum dots for fast pseudocapacitor and electrochromic applications, Adv. Mater. 26 (2014) 4260–4267.
[31] C. Bigey, L. Hilaire, G. Maire, Catalysis on Pd/WO_3 and Pd/WO_2: effect of the modifications of the surface states due to redox treatments on the skeletal rearrangement of hydrocarbons, J. Catal. 184 (1999) 406–420.
[32] M. Qiu, P. Sun, L. Shen, K. Wang, S. Song, X. Yu, S. Tan, C. Zhao, W. Mai, WO3 nanoflowers with excellent pseudo-capacitive performance and the capacitance

contribution analysis, J. Mater. Chem. 4 (2016) 7266–7273.
[33] H. Pang, B. Zhang, J. Du, J. Chen, J. Zhang, S. Li, Porous nickel oxide nanospindles with huge specific capacitance and long-life cycle, RSC Adv. 2 (2012) 2257–2261.
[34] H. Jiang, T. Zhao, C. Li, J. Ma, Hierarchical self-assembly of ultrathin nickel hydroxide nanoflakes for high-performance supercapacitors, J. Mater. Chem. 21 (2011) 3818–3823.
[35] H. Xu, Z. Hu, A. Lu, Y. Hu, L. Li, Y. Yang, Z. Zhang, H. Wu, Synthesis and super capacitance of goethite/reduced graphene oxide for supercapacitors, Mater. Chem. Phys. 141 (2013) 310–317.
[36] T. Brousse, D. Bêlanger, J.W. Long, To Be or not to Be pseudocapacitive? J. Electrochem. Soc. 162 (5) (2015) A5185–A5189.
[37] H.-S. Kim, J.B. Cook, H. Lin, J.S. Ko, S.H. Tolbert, V. Ozolins, B. Dunn, Oxygen vacancies enhance pseudocapacitive charge storage properties of MoO_{3-x}, Nat. Mater. 16 (2017) 454–460.